Contents lists available at ScienceDirect

Materials Today Bio

journal homepage: www.journals.elsevier.com/materials-today-bio

Cancer cell membrane-coated upconversion nanoparticles/$Zn_xMn_{1-x}S$ core-shell nanoparticles for targeted photodynamic and chemodynamic therapy of pancreatic cancer

Xiaoyan Liu [a,b,c,1], Zhaoyou Chu [d,e,1], Benjin Chen [d,e], Yan Ma [e], Lingling Xu [e,***],
Haisheng Qian [e,**], Yue Yu [a,b,*]

[a] *Cheeloo College of Medicine, Shandong University, Jinan, Shandong, 250012, PR China*
[b] *Department of Gastroenterology, The First Affiliated Hospital of USTC, Division of Life Sciences and Medicine, University of Science and Technology of China, Hefei, Anhui, 230001, PR China*
[c] *Department of Gastroenterology, The Lu'an Hospital Affiliated to Anhui Medical University, The Lu'an People's Hospital, Lu'an, Anhui, 237000, PR China*
[d] *Department of Pharmacology, School of Basic Medical Sciences, Anhui Medical University, Hefei, Anhui, 230032, PR China*
[e] *School of Biomedical Engineering, Anhui Provincial Institute of Translational Medicine, Anhui Medical University, Hefei, 230032, PR China*

ARTICLE INFO

ABSTRACT

Oxidative stress induced by reactive oxygen species (ROS) is promising treatment approach for pancreatic ductal adenocarcinoma (PDAC), which is typically insensitive to conventional chemotherapy. In this study, BxPC-3 pancreatic cancer cell membrane-coated upconversion nanoparticles/$Zn_xMn_{1-x}S$ core-shell nanoparticles (abbreviated as BUC@ZMS) were developed for tumor-targeted cancer therapy *via* synergistically oxidative stress and overcoming glutathione (GSH) overexpression. Using a combination of photodynamic therapy (PDT) and chemodynamic therapy (CDT), the BUC@ZMS core-shell nanoparticles were able to elicit the death of pancreatic cancer cells through the high production of ROS. Additionally, the BUC@ZMS core-shell nanoparticles could deplete intracellular GSH and increase the sensitivity of tumor cells to oxidative stress. The *in vivo* results indicated that BUC@ZMS nanoparticles can accumulate specifically in tumor locations and suppress PDAC without generating obvious toxicity. Thus, it was determined that the as-prepared core-shell nanoparticles would be a viable treatment option for solid malignancies.

1. Introduction

Pancreatic ductal adenocarcinoma (PDAC) is among the most aggressive malignancies, with a 5-year survival rate of 9% [1]. The poor prognosis stems from the advanced stage of the disease at diagnosis, the loss of surgical alternatives, and the limited sensitivity and efficacy of traditional chemotherapeutic regimens [2,3]. Therefore, it is imperative to develop more effective and safer treatments for PDAC. In 90% of cases of PDAC, oncogenic mutations of KRAS (a protein family implicated in cell signaling pathways) are identified [4]. These alterations result in the production of ROS at levels lower than those that cause senescence or cell death, but that are conducive to tumor growth and progression, therefore causing endogenous tolerance to first-line chemotherapeutics [5,6]. In an extreme scenario, however, excessive ROS accumulation can induce pancreatic cancer cell death [7,8]. Consequently, ROS-based therapies such as photodynamic [9], chemodynamic [10,11], and sonodynamic therapies [12] have recently been developed to address PDAC therapeutic challenges.

Photodynamic therapy (PDT) has came into view as a prospective alternative therapy for patients with unresectable pancreatic cancer due to its efficacy against chemotherapy-resistant and radio-resistant cells [13]. Nevertheless, PDT frequently confronts the issue of low efficiency

brought on by solid tumor hypoxia. A promising therapeutic approach for PDAC involves further boosting already raised ROS levels over the threshold necessary for cytotoxicity [7,8]. Chemodynamic therapy (CDT) can transforms H_2O_2 into highly cytotoxic hydroxyl radicals (•OH) through Fenton/Fenton-like reaction to produce more ROS and trigger severe oxidative damage for cancer synergistic therapy [14,15]. Moreover, CDT can overcome the limitation of tissue depth and hypoxia in tumor microenvironment (TME) [16,17]. Chen et al. application of CDT to PDAC revealed that the nanocomplex specifically stimulated the Fenton reaction to induce oxidative damage to cancer cells and suppress tumor growth without observable adverse effects [18]. Therefore, increasing ROS levels to achieve the synergistic impact of PDT and CDT in this study may be able to overcome pancreatic cancer cells' intrinsic resistance.

In this work, the core-shell nanoparticles comprised of upconversion nanoparticles (UCNPs) and $Zn_xMn_{1-x}S$ (abbreviated as ZMS) was proposed to fabricated firstly, which would be coated with BxPC-3 pancreatic cancer cell membrane (denoted as BUC@ZMS) for improved homologous targeting and combination therapies of pancreatic tumors (Scheme 1). The UCNPs give emissions in the ultraviolet (UV) light under 980 nm laser irradiation [19,20], would can be excited the shell (ZMS) to produce ROS *via* fluorescence resonance energy transfer (FRET) [21–23]. The shell of ZMS could react with H_2O_2 in the tumor's slightly acidic environment to form cytotoxic •OH, while synergistic consumption of intracellular glutathione (GSH) reduces •OH elimination and enhances the Fenton-like reaction efficiency. BUC@ZMS was transported to tumor tissues by homologous targeting of cancer cell membrane, displaying high tumor tissue targeting and converting the restricted passive endocytosis of nanoparticles to active targeting, which is expected to accomplish tumor precision therapy. As expected, under the homologous targeting effect on pancreatic cancer, the oxidative stress induced by PDT/CDT synergy and the effect on overcoming GSH overexpression are effective in the treatment of PDAC.

2. Materials and methods

2.1. Materials

Our group proposed a sequential growth protocol for generating $NaYF_4$:Yb (30%), Tm (0.5%)@$NaYF_4$ (abbreviated as UCNPs) core-shell nanoparticles, UCNPs@ZnO and UCNPs@ZnS nanoparticles with good dispersibility [24].

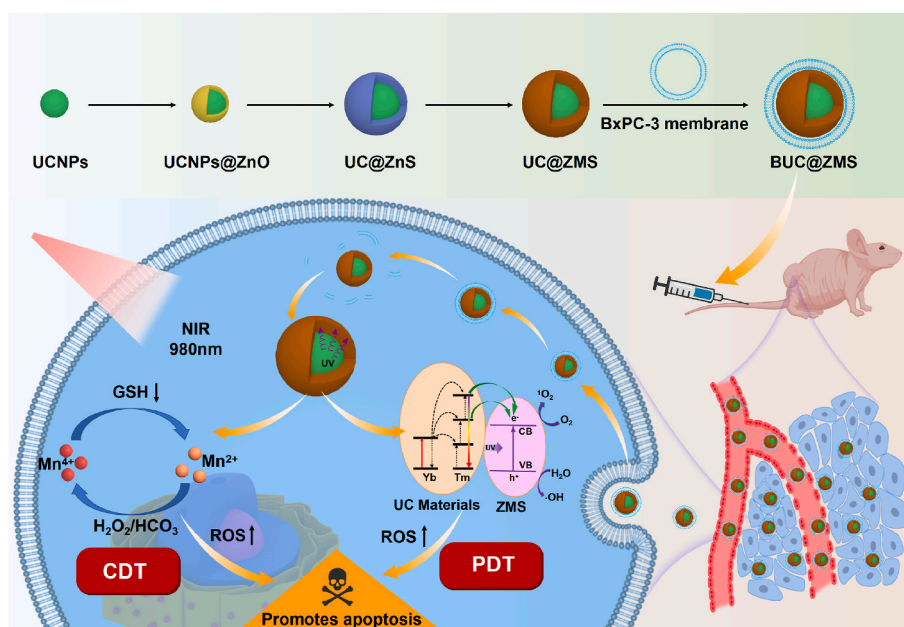### 2.2. Synthesis of UC@ZMS core-shell nanoparticles

A classic approach included adding 0.45 mmol of UCNPs@ZnS to 30 mL of ethylene glycol solution containing 0.45 mmol of manganese acetate, followed by stirring for 20 min. After that, 1 mL ammonia and 0.45 mmol L-cysteine were added to the aforesaid mixture and stirred continuously for 60 min to generate brownish yellow solution milky dispersion. The above solution was then transferred to the reaction kettle and reacted at 120 °C for 2 h.

2.3. Preparation and characterization of BUC@ZMS

Cell membrane of BxPC-3 were extracted according to previous research with some modifications [25,26]. The cancer cell membrane coated UC@ZMS was obtained by direct extrusion. A mixture of BxPC-3 cell membrane and UC@ZMS was extruded from a liposome extruder loaded with 400 nm polycarbonate membrane to produce membrane-modified UC@ZMS (abbreviated BUC@ZMS). Protein profiles of the obtained BxPC-3 cell membranes, BxPC-3 cancer cell and BUC@ZMS were extracted with RIPA buffer and were analyzed by the sodium dodecyl sulfate polyacrylamide gel electrophoresis (SDS-PAGE). After being stained with Coomassie brilliant blue, rinse with deionized water for observation and imaging of the electrophoresis gel. ChemiDoc XRS was used to obtain the band images. Western blot analysis was used to identify specific protein markers present on the cell membrane. Briefly, the sample lysates obtained from the cells were electrophoretically separated and transferred to polyvinylidene difluoride (PVDF) membranes (MerckMinipore, IPVH00010). 1% BSA blocking solution was applied to block the membrane for 2 h, followed by overnight incubation with an anti-Na^+/K^+-ATPase primary antibody at 4 °C. Secondary antibodies were then used to bind to the primary antibody.

2.4. Characterizations

The nanoparticles were characterized for surface morphology, phase, X-ray photoelectron spectra (XPS), X-ray diffraction (XRD), chemical composition, crystal phase, fluorescence and optical properties based on

Scheme 1. Schematic illustration of BUC@ZMS core-shell nanoparticles designed for synergetic PDT/CDT and tumor-targeted therapy for pancreatic cancer model.

our previous protocols or instruments [24,27]. Hitachi U-5100 spectrophotometer (Hitachi High-Technology Corporation) was used to detect UV–Vis–NIR absorption spectra. The morphology of UC@ZMS and BUC@ZMS were obtained by transmission electron microscope (TEM). The particle size and zeta potential were measured by dynamic light scattering at room temperature. Fluorescence images were recorded using a confocal laser scanning microscope (CLSM) (LMS-800, Carl Zeiss). All animal experiments were authorized by the Ethical Committee of Anhui Medical University (approval number: LLSC20210077).

2.5. Ability of BUC@ZMS to target homologous cancer cells

UC@ZMS or BUC@ZMS was labeled with Cy5.5 (UC@ZMS-Cy5.5 or BUC@ZMS-Cy5.5) to evaluate the targeting potential of BUC@ZMS for homologous tumor cells, and CLSM was performed to evaluate the absorption of BUC@ZMS-Cy5.5 by different cell lines. A density of 10^5 cells per dish of cells (BxPC-3, 3T3, 4T1 and PANC-1) were seeded into confocal culture dishes respectively and incubated overnight, fresh medium containing UC@ZMS-Cy5.5 or BUC@ZMS-Cy5.5 at gradient concentrations (25, 50, 75, μg mL^{-1}) was used to replace the medium and incubated for 4 h. After gently washing the cells three times with pre-cooled PBS, the treated cells nuclei were counterstained with DAPI, and Cy5.5 fluorescence was detected using CLSM. Fluorescence intensity was analyzed using Image j8.0. The fluorescence intensity of varied concentrations (25, 50, 75, μg mL^{-1}) of BUC@ZMS-Cy5.5 endocytosed by BxPC-3 cells was assessed by flow cytometry. A density of 5×10^4 cells per well of BxPC-3 cells were inoculated into 6-well plates and incubated for 18 h. Following that, fresh medium with varyings doses of BUC@ZMS-Cy5.5 was introduced and incubated for another 4 h. Before the fluorescence intensity of Cy5.5 was measured by flow cytometry, the collected processed cells were gently washed three times with pre-cooled PBS.

2.6. Cytotoxicity experiment

A CCK8 test was used to determine the cytotoxicity of BUC@ZMS against 3T3, HUVECs and BxPC-3 cells, which were used as control and tumor cell models, respectively. The cells were inoculated into 96-well plates with a density of 10^4 cells per well for cytotoxicity test. After 24 h of culturing, replace the culture medium with 10% FBS-medium containing UC@ZMS or BUC@ZMS in dose series concentrations (0, 12.5, 25, 50, 100, and 150 μg mL^{-1}), and culture media as the control group. For PDT or CDT groups or PDT combined with CDT groups, cells were incubated with BUC@ZMS for 4 h before prior to exposure to NIR laser irradiation (980 nm, 1 W cm^{-2}) for 3 min or/and H$_2$O$_2$ (100 μM) treatment. After continued incubation for 24 h, cells were incubated with Cell Counting Kit-8 (GLPBIO Co. Ltd) for 2 h, and the absorbance value at 450 nm was measured to estimate cell viability.

2.7. Apoptosis

Cell apoptosis was quantitatively observed by flow cytometry. A density of 10^5 cells/well of BxPC-3 cells was inoculated on 6-well plates and incubated for 24 h. The cells were subsequently cultured with new media containing BUC@ZMS (50 μg mL^{-1}) for 4 h, then incubated with or without H$_2$O$_2$ (100 μM) for 2 h, then irradiated with 980 nm laser (1 W cm^{-2}) or without irradiation for 3 min, and then incubated with fresh medium for 12 h. After the cells were digested and collected, the Annexin V-FITC/PI labeled cells were detected by flow cytometry and the apoptosis rate was calculated.

2.8. In vitro ROS measurement

2′,7′-Dichlorofluorescein diacetate (DCFH-DA) (Beyotime, China) was used to detecte intracellular ROS production. A density of 10^5 cells/dish of BxPC-3 cells was seeded into confocal culture dishes and incubated overnight. After a further 4 h of incubation with fresh DMEM media containing BUC@ZMS (100 μg mL^{-1}), the cells were subsequently incubated with or without H$_2$O$_2$ (100 μM) for 2 h and exposed or not to NIR (980 nm, 1 W cm^{-2}, 3 min). Following that, to produce a green fluorescent material (DCF), the cells were treated with DCFH-DA (10 μM) for 30 min. Free DCFH-DA was completely removed by gentle washing with PBS, followed by the confocal imaging of the intracellular green fluorescence with CLSM after DAPI staining (Beyotime, China).

2.9. In vivo antitumor therapeutic efficacy

BxPC-3 tumor-bearing mice were randomized divided into six groups at random and received the following treatments once their tumor volume reached about 100 mm^3: (1) PBS (control group), (2) PBS + NIR (placebo control group), (3) BUC@ZMS (CDT and homologous target group), (4) BUC@ZMS +0.5 W cm^{-2} NIR (PDT combine CDT and homologous target group), (5) RUC@ZMS +1 W cm^{-2} NIR (PDT combine CDT group), and (6) BUC@ZMS +1.0 W cm^{-2} NIR (PDT-enhanced combine CDT and homologous target group). A dose of 10 mg kg^{-1} of NP was given to the mice, and the (4), (5) and (6) groups were irradiated with NIR (980 nm, 1 W cm^{-2}) for 10 min at 4 h after injection. The mice body temperatures were monitored and kept below 38 °C throughout the exposure with an infrared thermal imaging camera. Tumor volume and weight were assessed every 2 days in all mice. On the 14th day after treatment, all mice were sacrificed, and the tumor tissues were stained with H&E, TUNEL and Ki-67, and the major organs were stained with H&E.

3. Results and discussion

3.1. Synthesis and characterization of UC@ZMS nanoparticles

Fig. 1a shows the formation process of BUC@ZMS nanoparticles. The core-shell nanoparticles were verified by TEM. Based on our previous study, NaYF$_4$:Yb/Tm@NaYF$_4$ upconversion nanoparticles were synthesized with uniform morphology and excellent dispersion, as shown in Fig. 1b [24]. UC@ZMS core-shell nanoparticles were synthesized as homogenous spherical structures with an average diameter of approximately 100 nm, with UCNPs in the core and ZMS wrapped around UCNPs as the shell (Fig. 1c). Fig. 1d–i illustrates the elemental distribution of the core-shell nanoparticles using elemental mapping images. Mn, Zn, and S elements were distributed throughout the entire shell layers of the core-shell nanoparticles, and Y element was distributed in the inner core, indicating that the particles had a 50 nm-diameter, hexagonal UCNPs nucleus and a 25 nm-thick ZMS shell. Sharp peaks of the ZMS phase (JCPDs 32–0635) emerged together with the characteristic peaks of UCNPs (JCPDs 28–1192), as shown by XRD (Fig. 1j), indicating a successful coating of the ZMS shell [24]. Moreover, the electronic states of UC@ZMS were studied using XPS, and the overall survey revealed that all of the elements of UC@ZMS existed (Fig. S1). A peak related to Mn 3s orbital are observed at 88.75 eV and 83.25 eV, in Fig. 1k. The ΔE of the 3s orbital of Mn was 5.5 eV, indicating that the element existed as Mn^{4+} [28]. From Fig. 1l, the average hydrodynamic size of UC@ZMS measured by dynamic light scattering (DLS) was about 149 nm.

3.2. Characterizes the ROS production of UC@ZMS core-shell NPs and the properties of BUC@ZMS

Previous studies have shown that composite nanostructures incorporated UCNPs and photosensitizers (PSs) can produce desired ROS when exposed to NIR laser light because the selective PSs have excitation bands that match the UCNPs emission range [29]. Additionally, when exposed to near-infrared light, the emitted energy can be transferred from the UCNPs core to the PSs shell to excite the PSs by FRET [30,31]. Substantial overlap exists between the ZMS absorption bands
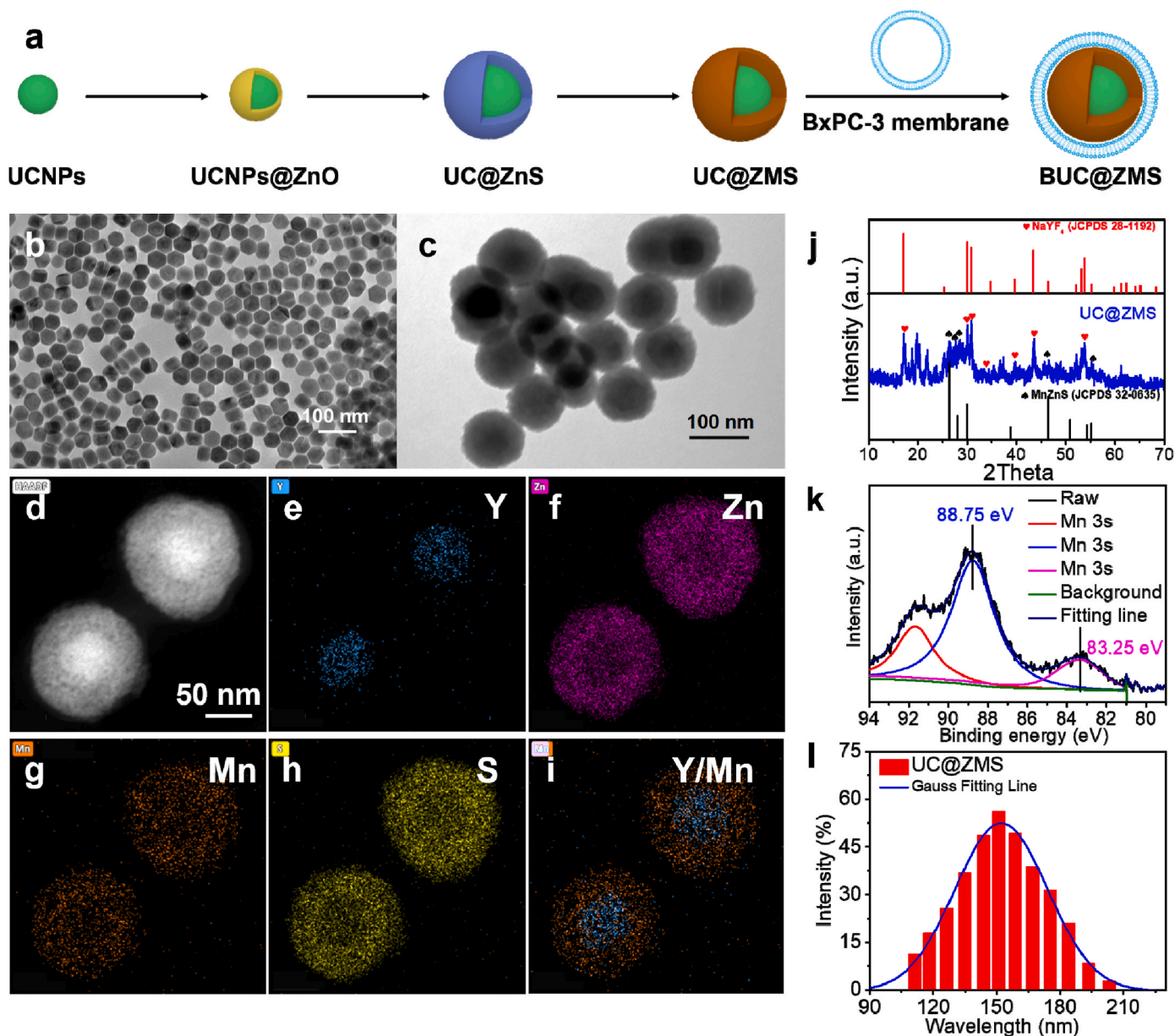
Fig. 1. (a) Schematic diagram of a synthetic of BUC@ZMS nanoparticles. (b, c) TEM images of NaYF$_4$:Yb/Tm@NaYF$_4$ upconversion nanoparticles and UC@ZMS core-shell nanoparticles, respectively. (d–i) Elemental mapping images of Y, Zn, Mn, S, and merged image of UC@ZMS core-shell NPs. (j) XRD pattern of UC@ZMS core-shell nanoparticles. (k) The survey of XPS of UC@ZMS (Mn 3s). (l) The size distributions of the UC@ZMS.

and the UCNP emission peaks. Particularly, the intensity of emission at about 361 nm nearly completely disappears due to the significant absorption of ZMS, and we observed that the fluorescence lifetime of UC@ZMS was significantly decrease compared with that of UCNP, which may be the result of enhanced FRET efficiency between the UCNP cores and ZMS shells (Fig. 2a and b and Fig. S2). [24]. UC@ZMS has considerably lower upconversion fluorescence than UCNPs, indicating that energy is transferred from UCNPs to the ZMS shell, which generates ROS by absorbing UV radiation. ZMS substantially quenched the emission intensity of UC@ZMS upconversion fluorescence, potentially producing cytotoxic singlet oxygen ($^1O_2$). UV–Vis absorption at 400–600 nm of the prepared UC@ZMS core-shell nanoparticles enhances the overlap between the fluorescence spectrum of UCNPs and ZMS absorption spectrum, resulting in reduced photo luminescence (PL) emissions of UCNPs *via* FRET process and increased •OH generation amount of ZMS under irradiation of NIR light [32,33].

Under 980 nm NIR laser irradiation, UC@ZMS NPs were exposed to

the photocatalytic decomposition of methylene blue (MB), demonstrating that ZMS shells formed on UCNPs are photocatalytically active. As shown in Fig. 2c, following near-infrared laser stimulation, the color of MB decreased, showing that the ZMS shell has excellent photocatalytic activity for MB. As catalytic nanomedicines, manganese-based nanostructures are sensitive to TME, contribute to TME-mediated Fenton/Fenton-like reactions, catalyze overexpressed H_2O_2 to produce •OH at the tumor site, and induce tumor cell death [34]. It was verified by fluorescence spectra that UC@ZMS exhibits Fenton-like reactivity by utilizing terephthalic acid (TAOH) as a detection probe to identify the formation of •OH. A high fluorescence peak at 425 nm suggested that a significant quantity of •OH was generated (Fig. 2d). We explored UC@ZMS at different pH values through the 3,5,3,5-Tetramethylbenzidine (TMB) probe, UC@ZMS showed good TMB oxidation ability at pH = 4 (Fig. S3). Accordingly, UC@ZMS demonstrated peroxidase-mimicking catalytic activity to produce ROS in the presence of H_2O_2 under acidic conditions. The results indicated that UC@ZMS
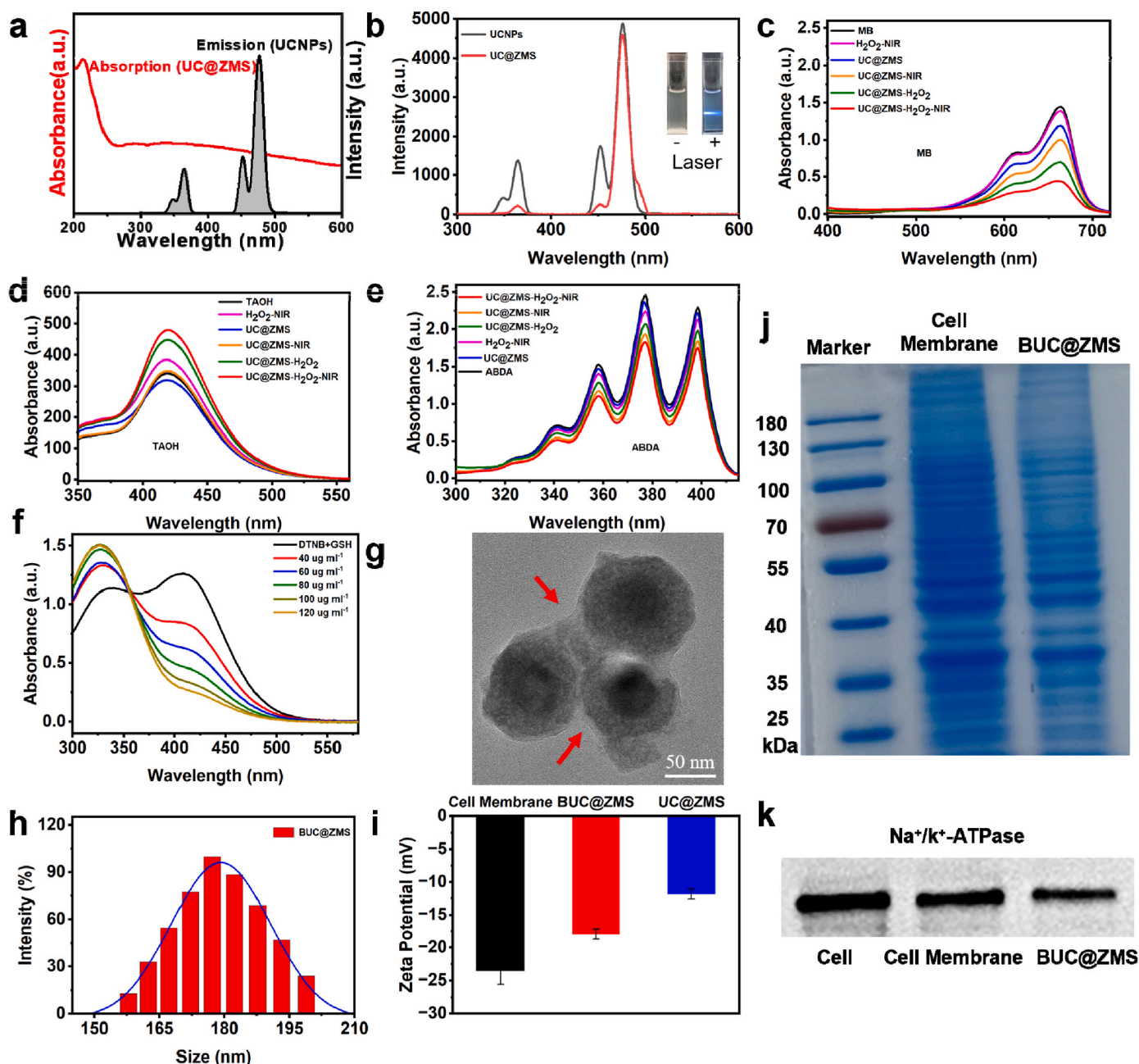
Fig. 2. (a) UV–Vis absorption spectrum of UC@ZMS core-shell nanoparticles overlapping with UCNP fluorescence spectrum. (b) Fluorescence spectra of UCNPs and UC@ZMS core-shell nanoparticles and the corresponding digital photographs. (c) Absorbance changes of MB at 650 nm. (d) Intensity changes of TAOH at 425 nm. (e) The absorbance changes of ABDA at 380 nm under different treatments in the presence of UC@ZMS. (f) Concentration-dependent GSH consumption by UC@ZMS. (g) TEM image of BUC@ZMS core-shell nanoparticles. (h) The size distributions of the BUC@ZMS; (i) BxPC-3 cell membrane, BUC@ZMS and UC@ZMS's Zeta potential. (j) Protein expression of BxPC-3 cell membrane and BUC@ZMS. (k) Protein expression of BxPC-3 cells, cell membrane and BUC@ZMS were detected by Western blot.

was capable of triggering Fenton-like reactions efficiently [35,36]. These properties conferred the controllability of UC@ZMS to initiate Fenton-like reactions in tumor cells but not in other cells, which provided a prerequisite for the application of CDT in PDAC therapy. The formation of $^1O_2$ was identified by 9,10-anthracenediyl-bis (methylene) dimalonic acid (ABDA). The absorbance intensity rose after adding UC@ZMS and irradiating the solution with a 980 nm laser, proving that $^1O_2$ generated from the activated ZMS (Fig. 2e). To summarize, these results demonstrated that UC@ZMS was successfully synthesize with the capability to generate $^1O_2$ under 980 nm laser irradiation and accumulate •OH under acidic conditions via Fenton-like reactions. GSH, an endogenous antioxidant, has been shown to maintain redox balance in cells and to suppress ROS-induced apoptosis. As reductive Mn^{4+} redox

could consumed intracellular GSH, thus disrupting the natural antioxidant defense system (ADS) to improve CDT effect [37]. In addition, ZMS acting as an oxidant could improve photodynamic efficiency by consuming intracellular GSH [38]. 5,50-dithio-bis (2-itrobenzoic acid) (DTNB) was used to investigate the GSH-depleting properties of UC@ZMS [39]. With the increase of UC@ZMS concentration, the characteristic peak of DTNB at 412 nm gradually decreases, indicating that UC@ZMS has a great capacity to utilize GSH (Fig. 2f).

The cancer membrane coating on the nanoparticles was verified by TEM. As depicted in Fig. 2g, the UC@ZMS cores are covered around by a BxPC-3 cell membrane. The average size of BUC@ZMS NPs as assessed by DLS was around 179 nm, as shown in Fig. 2h and Fig. S4. After BxPC-3 cell membrane was inserted successfully, the zeta potential of

BUC@ZMS was -17.98 ± 0.74 mV compared with UC@ZMS (-11.85 ± 0.77 mV), which was closer to that of pure BxPC-3 cell membrane (-23.57 ± 1.99 mV) (Fig. 2i). As shown in Fig. 2j and k, similar protein profiles were found in BUC@ZMS and BxPC-3 cell membranes. Moreover, BUC@ZMS was shown to have the cell membrane protein Na$^+$/K$^+$-ATPase by Western blot. The results manifested that the cell membrane of BxPC-3 human pancreatic cancer cell was successfully extracted and modified on UC@ZMS surface. According to the above results, BUC@ZMS NPs were effectively synthesized. Finally, ROS related probes (MB, TAOH, ABDA, and DTNB) were also used to investigate the production of ROS and the consumption of GSH in BUC@ZMS, and the results showed corresponding ROS production and GSH depletion (Fig. S5).

3.3. In vitro homologous targeting of BUC@ZMS

NPs only function as antitumor agents when they infiltrate tumor cells. Previous studies showed that cell membrane biomimetic nanoparticles outperformed conventional medication delivery methods at targeting homologous tumors [40,41]. We demonstrated that BUC@ZMS contains BxPC-3 cell membrane proteins (Fig. 2j and k). Flow cytometry and CLSM were applied to detect endocytosis in BUC@ZMS
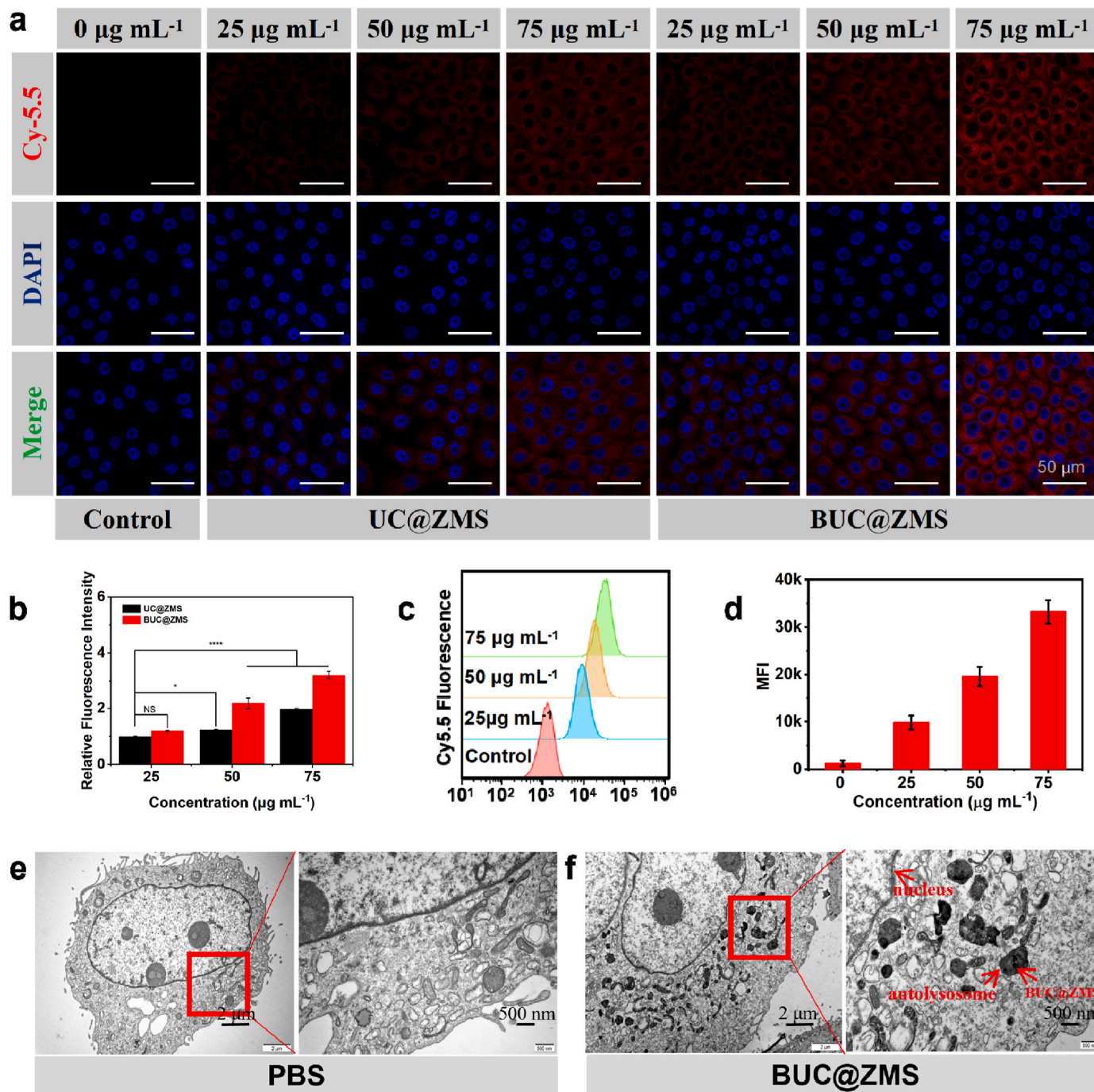

Fig. 3. (a,b) CLSM images and fluorescence intensity analysis of BxPC-3 cells after a 4 h incubation with UC@ZMS or BUC@ZMS at various concentrations. Scale bar = 50 μm. (c, d) Detected the uptake of BUC@ZMS at various concentrations by BxPC-3 cells after 4 h of incubation by FCM, and the mean fluorescence intensity of Cy5.5. (e, f) Bio-TEM images and local magnification images of BxPC-3 cells incubated with PBS and BUC@ZMS for 24 h. The experimental results were analyzed with mean $\pm$ SD (n = 3). *P < 0.05, **P < 0.01, ***P < 0.001, ****P < 0.0001.

loaded with Cy5.5 red fuel. To investigate the targeting specificity of BUC@ZMS, CLSM images were used to assess its absorption by homologous BxPC-3 cells (Fig. 3a) and non-homologous 4T1, 3T3, and Panc1 cells (Fig. S6a). After 4 h of NPs culture in BxPC-3 cells, fluorescence intensity increased with increasing NP concentrations (Fig. 3b), as validated by flow cytometry and fluorescence intensity analyses (Fig. 3c and d). BUC@ZMS induced stronger fluorescence than UC@ZMS at the same concentration, possibly because BUC@ZMS exhibited a higher degree of cellular internalization than UC@ZMS (Fig. 3b, d). Nevertheless, non-homologous cells absorption of BUC@ZMS was lower in the presence of the same material concentration than homologous cells, and there was also little difference between the uptake of UC@ZMS and

BUC@ZMS by non-homologous cells (Fig. S6b). Our findings suggest that BUC@ZMS has tumor-targeting ability and can precisely distribute NPs to homologous tumor cells. Autophagosomes were observed by bio-TEM pictures, as the gold standard method for the determination of autophagy, it can be observed that BUC@ZMS may be swallowed into autophagosomes (Fig. 3e and f) [42]. BUC@ZMS may be internalized from outside the cell by endocytosis, or may be present inside the cell due to the formation of autophagy vacuoles.

3.4. *In vitro* PDT synergies with CDT

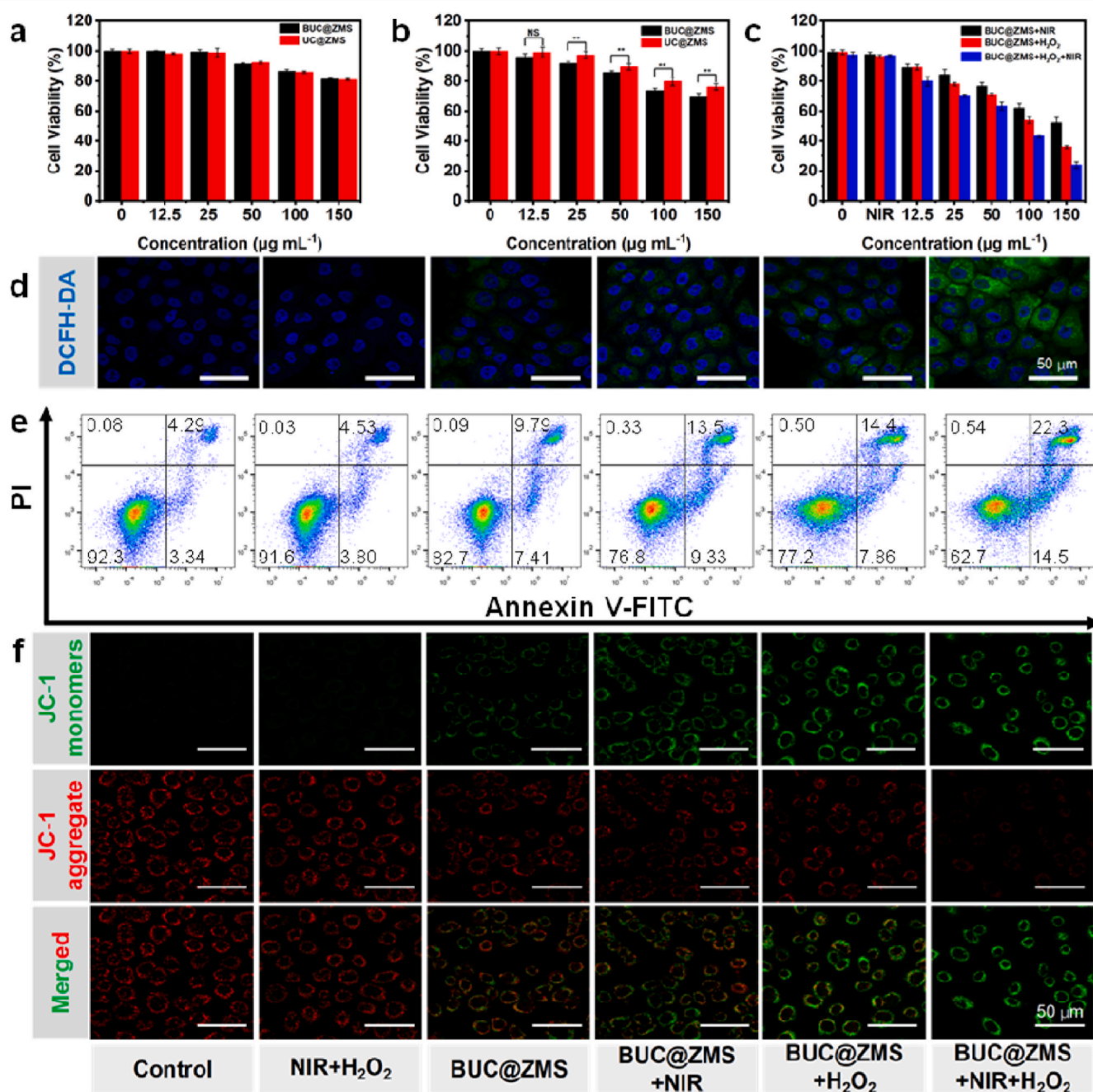After applying 3T3 cells and HUVEC cells as normal cell models to

Fig. 4. *In vitro* cytotoxicity of culture medium, various concentrations of UC@ZMS and BUC@ZMS on (a)3T3 cells, (b) BxPC-3 cells. (c) The apoptosis of BxPC-3 cells was induced by different treatments. (d) CLSM images showing different groups of BxPC-3 cells stained with DCFH-DA. (e) Annexin V-FITC/PI staining BxPC-3 cells, and the apoptosis of cells in different treatment groups was assessed by flow cytometry. (f) CLSM pictures indicate possible Mitochondrial membrane potential damage in several groups of BxPC-3 cells. The experimental results were analyzed with mean $\pm$ SD (n = 3). *P < 0.05, **P < 0.01, ***P < 0.001, ****P < 0.0001.

co-culture with NPs, CCK8 was utilized to test BUC@ZMS and UC@ZMS cytotoxicity in vitro [43]. Cell viability maintained above 85% under the treatment of 100 μg mL^{-1} of BUC@ZMS and UC@ZMS, as shown in Fig. 4a and Fig. S7a, demonstrating that NPs exhibit favorable in vitro biocompatibility. NPs, on the other hand, were shown to be more cytotoxic to BxPC-3 cells following co-incubation for 24 h (Fig. 4b), possibly because of the higher H_2O_2 concentration and acidic pH conditions of cancer cells' TME [44]. Moreover, this might explain some of the particular cytotoxicity of UC@ZMS against cancer cells. Surprisingly, BUC@ZMS was more cytotoxic to BxPC-3 cells than UC@ZMS, which might be attributed to BUC@ZMS targeting homologous BxPC-3 cells and BxPC-3 cells uptake of more BUC@ZMS. The ability of oxidative stress of BUC@ZMS as an anticancer agent on cell viability was assessed based on its strong PDT function, excellent Fenton-like activity, and homologous targeting of tumor cells. BxPC-3 cells treated with BUC@ZMS were substantially more toxic in the presence of H_2O_2 or/and 980 nm NIR irradiation than those treated with BUC@ZMS alone, indicating that the peroxidase-mimicking characteristics of UC@ZMS may be able to accelerate the conversion of H_2O_2 into extremely toxic ROS (Fig. 4c) [37]. UCNPs can transform low-energy near-infrared light into high-energy ultraviolet light, and the core-shell UC@ZMS has an excellent FRET efficiency between UCNPs core and ZMS shell. Excessive ROS lead to oxidative damage in cancer cells, may be the reasons for cancer cell cytotoxicity. 2′,7′-dichlorodihydrofluorescein diacetate (DCFH-DA) was used to assess the oxidative stress of BxPC-3 cells. CLSM results, shown in Fig. 4d, directly validated the formation of intracellular ROS, namely the non-fluorescent ROS probe DCFH was oxidized to green fluorescent DCF. DCF fluorescence emerged in the cells after incubation with BUC@ZMS, and the intracellular DCF fluorescence intensity was marginally raised when further co-incubated with H_2O_2 or irradiated with NIR laser. Furthermore, after treatment with BUC@ZMS combined with H_2O_2 and NIR irradiation for 3 min (980 nm, 1 W cm^{-2}), intracellular DCF fluorescence increased significantly (Figs. S7b and c), indicating that UC@ZMS can generate ROS in a simulated acidic TEM, and that NIR irradiation improved intracellular ROS generation. CLSM observations indicate that the peroxidase-mimicking ability of UC@ZMS can generate deadly ROS in cells, with laser irradiation enhancing this process. Apoptosis was identified by flow cytometry after cells were stained with Annexin V-fluorescein isothiocyanate/propidium iodide (FITC/PI) staining (Fig. 4e). Fig. S7d demonstrates that significant apoptotic cell populations appeared in the other four groups compared with the control and NIR + H_2O_2 groups, early and late apoptotic cell populations increased in the PDT group and CDT group after treatment. Furthermore, CDT combined with PDT significantly accelerated the apoptosis of BxPC-3 cells, indicating that the main mode of cell death in this investigation was apoptosis. To further explore the therapeutic effect of BUC@ZMS, calcein acetoxymethyl (AM)/PI experiments was applied to stain BxPC-3 live/dead cells (green/red fluorescence) (Fig. S8). The PDT and CDT groups displayed bright red fluorescence in contrast to the control and the NIR + H_2O_2 group, demonstrating that the CDT and PDT effects of BUC@ZMS were considerable. In the PDT combined with CDT group only red fluorescence was observed, suggesting nearly total cancer cell elimination. The inhibitory effect on BxPC-3 cells migration that treated with BUC@ZMS and BUC@ZMS + NIR (PDT) and BUC@ZMS + H_2O_2 (CDT) gradually increased after 24 h treatment in the same concentration compared to the control and H_2O_2+NIR groups, and the PDT combined with CDT group had the most significant relative scratch area ratio and the strongest inhibitory effect (Fig. S9). Moreover, results of CCK-8 matched those results.

ROS were produced during PDT and CDT treatments, interfering with electron transport chains and resulting in mitochondrial destruction [45,46]. Mitochondrial staining with JC-1 was used to investigate apoptosis mechanisms [46]. The mitochondrial status is determined by the variation in mitochondrial membrane potential (MMP, ΔΨm), and a reduction in MMP is indicative of early apoptosis, as indicated by the conversion of JC-1 from red to green fluorescence [47]. Fig. 4f reveals

that neither the control group nor the NIR + H_2O_2 group had green fluorescence; rather, a relatively high red fluorescence was found, suggesting that the cells were healthy. Nevertheless, green fluorescence appeared in the BUC@ZMS group, indicating that the uptake of BUC@ZMS by BxPC-3 cells decreased the membrane potential. Green fluorescence in the cells was greatly elevated after NIR laser irradiation, indicating PDT-induced early apoptosis, this is consistent with the cell death results shown by flow cytometry analysis (Fig. 4e). Fluorescence intensity was greater in the BUC@ZMS group when H_2O_2 was added to the media to imitate TEM, demonstrating that CDT lowered mitochondrial membrane potential and promoted apoptosis. The intensity of red fluorescence in mitochondria was greatly reduced in the BUC@ZMS combined with H_2O_2 and 980 nm NIR laser irradiation group, whereas the green fluorescence was significantly elevated in the cytoplasm. The alterations in CLSM images suggest that PDT combined with CDT might trigger apoptosis via the mitochondrial apoptotic pathway. The accumulated data suggest that there is crosstalk between apoptosis and autophagy [48], because autophagy is a lysosomal dependent process used to eliminate abnormal or damaged structures (e.g., protein aggregation or loss of mitochondrial membrane potential) [49], which is when the selective autophagy pathway is typically driven, leading to exposure of specific signals as "eat me", and then detected by autophagy receptors [50]. We observed the entry of nanomaterials into autophagosomes by bio-TEM (Fig. 3e and f), and found the Mitochondrial membrane potential damage in the BUC@ZMS group by JC-1 staining (Fig. 4f), and we have reasons to suspect that autophagy may occur. GSH is a major intracellular antioxidant [51]. In TME, high levels of GSH can reduce ROS produced by NPs, lowering the PDT and CDT therapeutic effect and severely restricting the utility of NPs in cancer treatment. Moreover, a decrease in GSH production promotes lethality in cancer cells harboring RAS oncogenes [52]. GSH levels were assessed in BxPC-3 cells using ThiolTracker^{TM} Violet [53]. As NPs concentration increased, as seen in Fig. S10, the intensity of green fluorescence gradually reduced in comparison to the control group, demonstrating that BUC@ZMS may efficiently deplete GSH in BxPC-3 cells, lessen antioxidant activity, and therefore improve the CDT effect. In addition, the BUC@ZMS group exhibited a lower fluorescence intensity than the UC@ZMS group at the same concentration, most likely because to the increased intracellular absorption of BUC@ZMS due to its homologous targeting of BxPC-3.

3.5. The anti-tumor ability of BUC@ZMS in vivo

Inspired by the remarkable therapeutic impact of BUC@ZMS on BxPC-3 cells in vitro, in vivo therapeutic efficacy was explored in nude mice harboring BxPC-3 tumors (Fig. 5a). Biosafety of BUC@ZMS was further evaluated. There was no significant change in blood biochemical tests between the treatment and the control group, proving that BUC@ZMS is biosafety at appropriate dosages (10 mg kg^{-1}) (Fig. S11a). H&E staining showed that there was no obvious injury or inflammation in major organs after 15 days of treatment (Fig. S11b).

Not only do the metabolism and biodistribution of NPs affect their effectiveness, but they also dictate their biosafety. In this study, we hypothesized that BUC@ZMS has homologous targeting capacity to BxPC-3 cancer cells in vivo. To assess the efficacy of passive targeting and homologous targeting, UC@ZMS and erythrocyte membrane-coated UCNPs (denoted as RUC@ZMS) served as control groups. BALB/c nude mice with BxPC-3 subcutaneous tumors were injected with PBS containing the same concentrations of BUC@ZMS, RUC@ZMS, or UC@ZMS via tail vein. To prevent the effects of liver uptake on the imaging of tumor areas, mouse models were injected with cancer cells in the lower limbs [54].

The cy5.5-labeled nanocomplex (BUC@ZMS-cy5.5) was utilized to obtain the fluorescence signal following injection to observe the distribution of BUC@ZMS within mice. The BUC@ZMS group's tumor location had the strongest fluorescence signal, indicating that BUC@ZMS
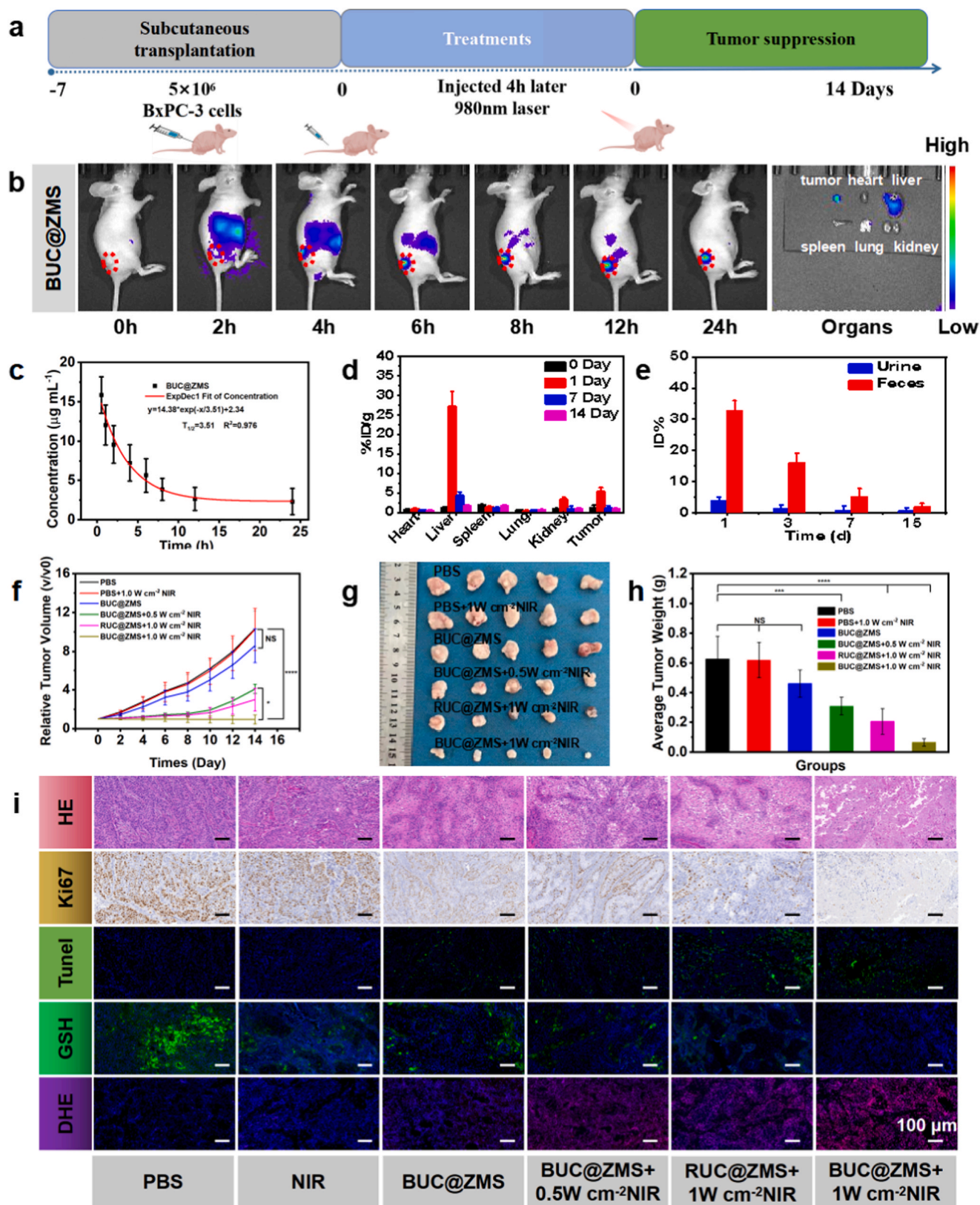
Fig. 5. (a) Schematic diagram of the procedure of anti-tumor therapy. (b) Imaging at various time points after iv injection of BUC@ZMS-cy5.5 (100 μL, 2 mg mL^{-1}) into BxPC-3 tumor-bearing mice. (c) Blood circulation duration following intravenous administration of BUC@ZMS in mice. (d, e) Biological distribution of Mn in major organs, tumors, urine, and feces at different times (0, 1, 7, and 14 days) after the administration of BUC@ZMS (n = 3). (f) Tumor relative growth curves. (g) Images of tumors resected in each of the treatment groups. (h) The average weight of excised tumors. (i) H&E, Ki67, TUNEL staining images of resected tumors on the 14th day, and images of GSH and DHE staining of resected tumors. The experimental results were analyzed with mean ± SD (n = 3). *P < 0.05, **P < 0.01, ***P < 0.001, ****P < 0.0001.

could target the BxPC-3 tumor by homologous binding (Fig. 5b, Fig. S12a). The liver is a prominent organ of the reticuloendothelial system (RES) that is abundant in phagocytes and can accumulate the most nanoparticles [55]. The BUC@ZMS group had less liver accumulation than the RUC@ZMS group, indicating that cell membrane coating of cancer cells could indeed reduce RES absorption. In addition to EPR effect, the tumor aggregation in RUC@ZMS group was more obvious than that in UC@ZMS group because RUC@ZMS was in circulation longer than UC@ZMS [56]. We introduced 4T1 subcutaneous tumor as the control group, and the results showed that BUC@ZMS was less enriched in the tumor area of 4T1 subcutaneous tumor than that of BxPC-3 subcutaneous tumor, which further verified that BUC@ZMS had homologous targeting to BxPC-3 subcutaneous tumor (Fig. S12b). Ex vivo fluorescence imaging was performed on tumors and major organs of mice sacrificed 24 h after injection. The maximum rate of tumor accumulation was seen following BUC@ZMS injection into BxPC-3 tumor bearing mice (Figs. S12c and d). *In vivo,* the prepared BUC@ZMS demonstrated a good homologous tumor targeting effect.

The pharmacokinetic data of Mn in blood samples at various time points (0, 0.5, 1, 2, 4, 6, 8, 12, 24 h) were identified by inductively coupled plasma-mass spectrometry (ICP-MS), and the half-life (T1/2) was determined to be 3.51 h (Fig. 5c). Because of the erythrocyte membrane lengthens RUC@ZMS's blood circulation time, RUC@ZMS has a longer half-life than UC@ZMS (Fig. S13), but it is still shorter than the blood circulation time of BUC@ZMS. It has been demonstrated that BUC@ZMS possesses lengthy blood circulation in addition to homologous tumor targeting [57]. At various time periods (2–24 h) following intravenous (iv) injection of BUC@ZMS, main organs and tumors were collected for ICP-MS analysis [22]. BUC@ZMS were found mostly in the liver and tumor sites, and gradually eliminated primarily in feces over time (Fig. 5d and e), which we attribute to hepatointestinal circulation. Pharmacokinetic and biodistribution investigations have shown that cancer cell membrane-coated UC@ZMS prolongs blood circulation and accumulates preferentially in homologous tumors.

Mice with tumor volume of ~100 mm^3 were randomly divided into six groups (n = 5), including the (1) PBS, (2) NIR, (3) BUC@ZMS, (4) BUC@ZMS+0.5 W cm^{-2} NIR, (5) RUC@ZMS+1 W cm^{-2} NIR, and (6) BUC@ZMS+1 W cm^{-2} NIR, to investigate the tumor therapeutic effect of the material *in vivo*. Prior to that, it's essential to investigate how materials that are injected affect the body weight of mice, which indicates how toxic they are to the mice's system. As shown in Fig. S14, the mice body weight showed a continuous rising trend over the course of 14 days, demonstrating that all five groups were safe for mice. Throughout the 14 days of therapy, the relative tumor volume of each cohort of mice was recorded on alternate days (Fig. 5f). The tumor model was successful, as shown by the mice in the PBS group who did not receive any treatment and gradually developed tumors. The tumor weights and volumes were comparable across the NIR and control groups, showing that NIR had no therapeutic impact on the tumors. The BUC@ZMS group (CDT group) had a decreased tumor volume than the control group, however the CDT impact did not entirely eradicate the tumors. PDT was introduced as a therapeutic approach to further improve tumor killing ability.

The BUC@ZMS+0.5 W cm^{-2} NIR group (PDT + CDT group), as compared to other groups (PBS, NIR, and BUC@ZMS), suppressed tumor development. As the intensity of NIR irradiation was increased, the BUC@ZMS+1 W cm^{-2} NIR group demonstrated the greatest reduction of tumor development (Fig. 5f). Similar results were obtained with tumor weight curve (Fig. 5h). After treatment with BUC@ZMS NPs under NIR laser irradiation, the results demonstrated a considerable inhibition of tumor development, indicating that the CDT and PDT effects of BUC@ZMS might cooperate to generate more ROS and, ultimately, kill tumors *in vivo*. While smaller than those in the BUC@ZMS +0.5 W cm^{-2} NIR group, tumor weight in the RUC@ZMS +1 W cm^{-2} NIR group was greater than those in the BUC@ZMS+1 W cm^{-2} NIR group. It is hypothesized that BUC@ZMS has a stronger tumor-targeting

capacity than RUC@ZMS, and tumor tissue uptakes more BUC@ZMS, indicating that BUC@ZMS has a favorable impact when CDT and PDT are combined. By increasing the power, however, the PDT impact of the RUC@ZMS+1 W cm^{-2} NIR group was amplified, thus the RUC@ZMS +1 W cm^{-2} NIR group suppresses cancers more effectively than the BUC@ZMS+0.5 W cm^{-2} NIR group. It demonstrates the effective PDT function of the core-shell structure of UC@ZMS.

Different groups of mice were dissected and their tumors were removed. Fig. 5g and h revealed intuitively that BUC@ZMS significantly suppressed tumor development under 1 W cm^{-2} NIR laser irradiation; nevertheless, tumor volume and weight rose higher in other experimental groups. Hematoxylin-eosin (H&E) and terminal deoxynucleotidyl transferase dUTP nick end labeling (TUNEL) tumor staining were performed to evaluate the killing effect on tumor cells, showed necrosis and apoptosis of tumor cells (Fig. 5i, Fig. S15), which was consistent with the previous conclusions [37].

According to H&E-staining images of tumor slices, BUC@ZMS+1 W cm^{-2} NIR group demonstrated the most substantial matrix degradation, cell fragmentation, and lysis, whereas the pure NIR laser group had little or no apparent apoptosis (Fig. 5i). Furthermore, TUNEL staining images showed that the tumor tissue in the BUC@ZMS+1 W cm^{-2} NIR group had the lowest level of Ki-67 proliferation and the highest level of apoptosis, demonstrating that BUC@ZMS has a beneficial therapeutic effect on the tumor tissue when exposed to 980 nm NIR laser irradiation (Fig. 5i). Oncogenic KRAS-containing cancer cells were suppressed by blocking glutathione production [52]. Moreover, immunofluorescence labeling was used to determine the level of GSH present at the tumor site, BUC@ZMS and BUC@ZMS + NIR groups exhibited weaker green fluorescence, indicating BUC@ZMS lowered antioxidant capacity and enhanced CDT effects in BxPC-3 cells by successfully depleting GSH (Fig. S16).

Through using Dihydroethidium (DHE) immunofluorescence labeling, we investigated the oxidative stress caused by BUC@ZMS in the tumor site. Surprisingly, tumor sections from mice treated with BUC@ZMS + NIR showed a bright red fluorescence, indicating the tumor tissue had a high amount of ROS, comparable to what was seen in cell research (Fig. S17). The aforesaid findings suggest that BUC@ZMS combined CDT and PDT actions might completely suppress tumor development, considerably enhancing therapeutic efficiency. Excellent biosafety is required for the use of nanoparticles in biomedicine. There were no noticeable pathological anomalies in the mice's main organs (Fig. S18), indicating that BUC@ZMS had a negligible deleterious effect on animals. Our findings fully support the use of BUC@ZMS as a safe and effective homologous targeting reagent in combination with PDT synergistic CDT for the treatment of pancreatic cancer.

4. Conclusions

In this research, we developed a tumor-targeted multifunctional BUC@ZMS core-shell nanostructure with synergistic PDT/CDT capabilities and the ability to combat GSH overexpression as an effective treatment agent for PDAC. The cancer cell membrane coating greatly enhanced the circulation and tumor-retention of UC@ZMS. The homologous tumor targeting effect of UC@ZMS core-shell nanomaterials coated with cancer cell membrane were confirmed by *in vitro* and *in vivo* experiments. The coexistence of multivalent Mn allows for the consumption of GSH, whereas the Fenton-like reaction of Mn^{2+} substantially increased ROS generation, hence decreasing the antioxidant and strengthening the CDT impact. Meanwhile, as a result of the FRET interaction between ZMS and UCNPs, large amounts of intracellular ROS were generated in response to NIR irradiation. The outcomes showed that BUC@ZMS effectively treated PDAC *in vitro* and *in vivo* via decreasing the level of GSH of the TEM and increasing the oxidative stress brought on by PDT/CDT combination. In conclusion, BUC@ZMS core-shell nanospheres have been suggested as an alternate strategy to generate high-performance, multifunctional composite nanostructures

for the combination therapy of pancreatic cancer.

Credit author statement

Xiaoyan Liu, Zhaoyou Chu, Benjin Chen, Haisheng Qian and Yue Yu conceived and designed the experiments. Xiaoyan Liu, Zhaoyou Chu, Benjin Chen performed experiments. Xiaoyan Liu, Zhaoyou Chu, Benjin Chen, Lingling Xu, Haisheng Qian and Yue Yu discussed the results. Xiaoyan Liu, Zhaoyou Chu, Lingling Xu, Haisheng Qian and Yue Yu wrote and revised the manuscript. All authors discussed the results and commented on the manuscript.

Declaration of competing interest

We declare that we have no business or personal relationships with other people or organizations to inappropriately influence our research. There is no professional or other personal interest of any nature or type in any product, service and/or company that could be construed to influence the position or scrutiny presented in the manuscript.

Data availability

Data will be made available on request.

Acknowledgment

Appendix A. Supplementary data

Supplementary data to this article can be found online at https://doi.org/10.1016/j.mtbio.2023.100765.

References

[1] R.L. Siegel, K.D. Miller, A. Jemal, Cancer statistics, 2020, CA cancer, J. Clin. 70 (2020) 7–30, https://doi.org/10.3322/caac.21590.

[2] J. Kleeff, M. Korc, M. Apte, C.L. Vecchia, C.D. Johnson, A.V. Biankin, R.E. Neale, M. Tempero, D.A. Tuveson, R.H. Hruban, J.P. Neoptolemos, Pancreatic cancer, Nat. Rev. Dis. Prim. 21 (2016), 16022, https://doi.org/10.1038/nrdp.2016.22.

[3] N. Marschner, S. Hegewisch-Becker, M. Reiser, E.v.d. Heyde, M. Bertram, S. H. Hollerbach, S. Kreher, T. Wolf, A. Binninger, M. Chiabudini, A. Kaiser-Osterhues, M. Jänicke, FOLFIRINOX or gemcitabine/nab-paclitaxel in advanced pancreatic adenocarcinoma: a novel validated prognostic score to facilitate treatment decision-making in real-world, Int. J. Cancer 152 (2023) 458–469, https://doi.org/10.1002/ijc.34271.

[4] K.M. Mann, H.Q. Ying, J. Juan, N.A. Jenkins, N.G. Copeland, KRAS-related proteins in pancreatic cancer, Pharmacol. Ther. 168 (2016) 29–42, https://doi.org/10.1016/j.pharmthera.2016.09.003.

[5] N. Santana-Codina, A.A. Roeth, Y. Zhang, A.N. Yang, O. Mashadova, J.M. Asara, X. W. Wang, R.T. Bronson, C.A. Lyssiotis, H.Q. Ying, A.C. Kimmelman, Oncogenic KRAS supports pancreatic cancer through regulation of nucleotide synthesis, Nat. Commun. 9 (2018) 4945, https://doi.org/10.1038/s41467-018-07472-8.

[6] G.Y. Liou, H. Döppler, K.E. DelGiorno, L.Z. Zhang, M. Leitges, H.C. Crawford, M. P. Murphy, P. Storz, Mutant KRAS-induced mitochondrial oxidative stress in acinar cells upregulates EGFR signaling to drive formation of pancreatic precancerous lesions, Cell Rep. 14 (2016) 2325–2336, https://doi.org/10.1016/j.celrep.2016.02.029.

[7] G. Rademaker, Y. Boumahd, R. Peiffer, S. Anania, T. Wissocq, M. Liégeois, G. Luis, N.E. Sounni, F. Agirman, N. Maloujahmoum, P.D. Tullio, M. Thiry, A. Bellahcène, V. Castronovo, O. Peulen, Myoferlin targeting triggers mitophagy and primes ferroptosis in pancreatic cancer cells, Redox Biol. 53 (2022), 102324, https://doi.org/10.1016/j.redox.2022.102324.

[8] S. Sarkar, D. Dutta, S.K. Samanta, K. Bhattacharya, B.C. Pal, J.P. Li, K. Datta, C. Mandal, C. Mandal, Oxidative inhibition of Hsp90 disrupts the super-chaperone complex and attenuates pancreatic adenocarcinoma *in vitro* and *in vivo*, Int. J. Cancer 132 (2013) 695–706, https://doi.org/10.1002/ijc.27687.

[9] H.Y. Yang, R.F. Liu, Y.X. Xu, L.X. Qian, Z.F. Dai, Photosensitizer nanoparticles boost photodynamic therapy for pancreatic cancer treatment, Nano-Micro Lett. 13 (2021) 35, https://doi.org/10.1007/s40820-020-00561-8.

[10] H.T. Sun, Y.Y. Zhang, S.Y. Chen, R.Z. Wang, Q. Chen, J.C. Li, Y. Luo, X.L. Wang, H. G. Chen, Photothermal Fenton nanocatalysts for synergetic cancer therapy in the second near-infrared window, ACS Appl. Mater. Interfaces 12 (2020) 30145–30154, https://doi.org/10.1021/acsami.0c07013.

[11] L. Li, Z. Yang, W.P. Fan, L.C. He, C. Cui, J.H. Zou, W. Tang, O. Jacobson, Z. T. Wang, G. Niu, S. Hu, X.Y. Chen, *In situ* polymerized hollow mesoporous organosilica biocatalysis nanoreactor for enhancing ROS-mediated anticancer therapy, Adv. Funct. Mater. 30 (2020), 1907716, https://doi.org/10.1002/adfm.201907716.

[12] R.J. Browning, S. Able, J.L. Ruan, L.a Bau, P.D. Allen, V. Kersemans, S. Wallington, P. Kinchesh, S. Smart, C. Kartsonaki, S. Kamila, K. Logan, M.A. Taylor, A. P. McHale, J.F. Callan, E. Stride, K.A. Vallis, Combining sonodynamic therapy with chemoradiation for the treatment of pancreatic cancer, J. Contr. Release 337 (2021) 371–377, https://doi.org/10.1016/j.jconrel.2021.07.020.

[13] H.C. Huang, S. Mallidi, J. Liu, C.T. Chiang, Z.M. Mai, R. Goldschmidt, N. Ebrahim-Zadeh, I. Rizvi, T. Hasan, Photodynamic therapy synergizes with irinotecan to overcome compensatory mechanisms and improve treatment outcomes in pancreatic cancer, Cancer Res. 76 (2016) 1066–1077, https://doi.org/10.1158/0008-5472.CAN-15-0391.

[14] T. Jia, Z. Wang, Q.Q. Sun, S.M. Dong, J.T. Xu, F.M. Zhang, L.L. Feng, F. He, D. Yang, P.P. Yang, J. Lin, Intelligent Fe-Mn layered double hydroxides nanosheets anchored with upconversion nanoparticles for oxygen-elevated synergetic therapy and bioimaging, Small 16 (2020), e2001343, https://doi.org/10.1002/smll.202001343.

[15] G. Guan, C. Zhang, H.Y. Liu, Y.J. Wang, Z. Dong, C. Lu, B. Nan, R.Y. Yue, X. Yin, X. B. Zhang, G.S. Song, Ternary alloy PtWMn as a Mn nanoreservoir for high-field MRI monitoring and highly selective ferroptosis therapy, Angew. Chem. Int. Ed. 61 (2022), e202117229, https://doi.org/10.1002/anie.202117229.

[16] T.L. Li, B. Rao, D. Xu, J. Zhou, W.B. Sun, X. Zhi, C.L. Zhang, D.X. Cui, H.B. Xu, Enzyme-like copper-encapsulating magnetic nanoassemblies for switchable T_1-weighted MRI and potentiating chemo-/photo-dynamic therapy, Acta Biomater. 153 (2022) 431–441, https://doi.org/10.1016/j.actbio.2022.09.062.

[17] Y.M. Wang, D. Wang, Y.Y. Zhang, H. Xu, L.X. Shen, J. Cheng, X.Y. Xu, H. Tan, X. Y. Chen, J.S. Li, Tumor microenvironment-adaptive nanoplatform synergistically enhances cascaded chemodynamic therapy, Bioact. Mater. 22 (2022) 239–253, https://doi.org/10.1016/j.bioactmat.2022.09.025.

[18] Y. Chen, Y.K. Huang, S.L. Zhou, M.L. Sun, L. Chen, J.H. Wang, M.J. Xu, S.S. Liu, K. F. Liang, Q. Zhang, T.Z. Jiang, Q.X. Song, G. Jiang, X.Y. Tang, X.L. Gao, J. Chen, Tailored chemodynamic nanomedicine improves pancreatic cancer treatment via controllable damaging neoplastic cells and reprogramming tumor microenvironment, Nano Lett. 20 (2020) 6780–6790, https://doi.org/10.1021/acs.nanolett.0c02622.

[19] X.W. Cheng, J. Zhou, J.Y. Yue, Y. Wei, C. Gao, X.J. Xie, L. Huang, Recent development in sensitizers for lanthanide-doped upconversion luminescence, Chem. Rev. 122 (2022) 15998–16050, https://doi.org/10.1021/acs.chemrev.1c00772.

[20] J. Shen, L. Zhao, G. Han, Lanthanide-doped upconverting luminescent nanoparticle platforms for optical imaging-guided drug delivery and therapy, Adv. Drug Deliv. Rev. 65 (2013) 744–755, https://doi.org/10.1016/j.addr.2012.05.007.

[21] Z.Y. Chu, T. Tian, Z.C. Tao, J. Yang, B.J. Chen, H. Chen, W.N. Wang, P.Q. Yin, X. P. Xia, H. Wang, H.S. Qian, Upconversion nanoparticles@AgBiS₂ core-shell nanoparticles with cancer-cell-specific cytotoxicity for combined photothermal and photodynamic therapy of cancers, Bioact. Mater. 17 (2022) 71–80, https://doi.org/10.1016/j.bioactmat.2022.01.010.

[22] Z.Y. Chu, H. Chen, P.S. Wang, W.N. Wang, J. Yang, J.N. Sun, B.J. Chen, T. Tian, Z. B. Zha, H. Wang, H.S. Qian, Phototherapy using a fluoroquinolone antibiotic drug to suppress tumor migration and proliferation and to enhance apoptosis, ACS Nano 16 (2022) 4917–4929, https://doi.org/10.1021/acsnano.2c00854.

[23] Y.C. Liu, L.L. Teng, B.L. Yin, H.M. Meng, X. Yin, S.Y. Huan, G.S. Song, X.B. Zhang, Chemical design of activatable photoacoustic probes for precise biomedical applications, Chem Rev 122 (2022) 6850–6918, https://doi.org/10.1021/acs.chemrev.1c00875.

[24] W.N. Wang, C.X. Huang, C.Y. Zhang, M.L. Zhao, J. Zhang, H.J. Chen, Z.B. Zha, T. T. Zhao, H.S. Qian, Controlled synthesis of upconverting nanoparticles/Zn$_x$Cd$_{1-x}$S yolk-shell nanoparticles for efficient photocatalysis driven by NIR light, Appl. Catal. B Environ. 224 (2017) 854–862, https://doi.org/10.1016/j.apcatb.2017.11.037.

[25] L. Rao, L.L. Bu, B. Cai, J.H. Xu, A. Li, W.F. Zhang, Z.J. Sun, S.S. Guo, W. Liu, T. H. Wang, X.Zh Zhao, Cancer cell membrane-coated upconversion nanoprobes for highly specific tumor imaging, Adv. Mater. 28 (2016) 3460–3466, https://doi.org/10.1002/adma.201506086.

[26] Y.L. Jia, X.B. Wang, D.H. Hu, P. Wang, Q.H. Liu, X.J. Zhang, J.Y. Jiang, X. Liu, Z. H. Sheng, B. Liu, H.R. Zheng, Phototheranostics: active targeting of orthotopic glioma using biomimetic proteolipid nanoparticles, ACS Nano 13 (2019) 386–398, https://doi.org/10.1021/acsnano.8b06556.

[27] B.J. Chen, C.Y. Zhang, W.N. Wang, Z.Y. Chu, Z.B. Zha, X.Y. He, W. Zhou, T. Liu, H. Wang, H.S. Qian, Ultrastable AgBiS₂ hollow nanospheres with cancer cell-specific cytotoxicity for multimodal tumor therapy, ACS Nano 14 (2020) 14919–14928, https://doi.org/10.1021/acsnano.0c04370.

[28] L.S. Lin, J.B. Song, L. Song, K.M. Ke, Y.J. Liu, Z.J. Zhou, Z.Y. Shen, J. Li, Z. Yang, W. Tang, G. Niu, H.H. Yang, X.Y. Chen, Simultaneous Fenton-like ion delivery and glutathione depletion by MnO₂-based nanoagent to enhance chemodynamic

therapy, Angew. Chem. Int. Ed. 57 (2018) 4902–4906, https://doi.org/10.1002/anie.201712027.

[29] Z.Y. Hou, Y.X. Zhang, K.R. Deng, Y.Y. Chen, X.J. Li, X.R. Deng, Z.Y. Cheng, H. Z. Lian, C.X. Li, J. Lin, UV-emitting upconversion-based TiO2 photosensitizing nanoplatform: near-infrared light mediated in vivo photodynamic therapy via mitochondria-involved apoptosis pathway, ACS Nano 9 (2015) 2584–2599, https://doi.org/10.1021/nn506107c.

[30] Y.W. Wang, Y.M. Li, Z.J. Zhang, L. Wang, D. Wang, B.Z. Tang, Triple-jump photodynamic theranostics: MnO2 combined upconversion nanoplatforms involving a type-I photosensitizer with aggregation-induced emission characteristics for potent cancer treatment, Adv. Mater. 33 (2021), e2103748, https://doi.org/10.1002/adma.202103748.

[31] L.L. Feng, D. Yang, F. He, S.L. Gai, C.X. Li, Y.L. Dai, P.P. Yang, A core-shell-satellite structured Fe3O4@g-C3N4-UCNPs-PEG for T1/T2-weighted dual-modal MRI-guided photodynamic therapy, Adv. Healthcare Mater. 6 (2017), https://doi.org/10.1002/adhm.201700502, 10.1002/adhm.201700502.

[32] C. Yao, W.X. Wang, P.Y. Wang, M.Y. Zhao, X.M. Li, F. Zhang, Near-infrared upconversion mesoporous cerium oxide hollow biophotocatalyst for concurrent pH-/H2O2-responsive O2-evolving synergetic cancer therapy, Adv. Mater. 30 (2018), https://doi.org/10.1002/adma.201704833.

[33] Z.Q. Li, X.C. Zou, F. Shi, R. Liu, Y. Yagci, Highly efficient dandelion-like near-infrared light photoinitiator for free radical and thiol-ene photopolymerizations, Nat. Commun. 10 (2019) 3560, https://doi.org/10.1038/s41467-019-11522-0.

[34] M. Su, Y. Zhu, J. Chen, B. Zhang, C. Sun, M. Chen, X. Yang, Microfluidic synthesis of manganese-alginate nanogels with self-supplying H2O2 capability for synergistic chemo/chemodynamic therapy and boosting anticancer immunity, Chem. Eng. J. 435 (2022), 134926, https://doi.org/10.1016/j.cej.2022.134926.

[35] Z.L. Dong, L.Z. Feng, Y. Chao, Y. Hao, M.C. Chen, F. Gong, X. Han, R. Zhang, L. Cheng, Z. Liu, Amplification of tumor oxidative stresses with liposomal Fenton catalyst and glutathione inhibitor for enhanced cancer chemotherapy and radiotherapy, Nano Lett. 19 (2019) 805–815, https://doi.org/10.1021/acs.nanolett.8b03905.

[36] C. Pan, M.T. Ou, Q.Z. Cheng, Y. Zhou, Y.K. Yu, Z.M. Li, F. Zhang, D.H. Xia, L. Mei, X.Y. Ji, Z-scheme heterojunction functionalized pyrite nanosheets for modulating tumor microenvironment and strengthening photo/chemodynamic therapeutic effects, Adv. Funct. Mater. 30 (2019), 1906466, https://doi.org/10.1002/adfm.201906466.

[37] J. Ruan, H. Liu, B.j. Chen, F. Wang, W.N. Wang, Z.B. Zha, H.S. Qian, Z.H. Miao, J. N. Sun, T. Tian, Y.L. He, H. Wang, Interfacially engineered ZnxMn1−xS@polydopamine hollow nanospheres for glutathione depleting photothermally enhanced chemodynamic therapy, ACS Nano 15 (2021) 11428–11440, https://doi.org/10.1021/acsnano.1c01077.

[38] H.H. Fan, G.B. Yan, Z.L. Zhao, X.X. Hu, W.H. Zhang, H. Liu, X.Y. Fu, T. Fu, X. B. Zhang, W.H. Tan, A smart photosensitizer-manganese dioxide nanosystem for enhanced photodynamic therapy by reducing glutathione levels in cancer cells, Angew. Chem. Int. Ed. 55 (2016) 5477–5482, https://doi.org/10.1002/anie.201510748.

[39] F.Y. Yu, X.W. Shang, Z.X. Wang, Y. Zhu, S.M. Chen, H. Yuan, F.Q. Hu, Drug-independent NADPH-consuming micelles collaborate with ROS-generator for cascade ferroptosis amplification by impairing redox homeostasis, Mater Today Bio 18 (2023), 100532, https://doi.org/10.1016/j.mtbio.2022.100532.

[40] H.P. Sun, J.H. Su, Q.S. Meng, Q. Yin, L.L. Chen, W.W. Gu, P.C. Zhang, Z.W. Zhang, H.J. Yu, S.L. Wang, Y.P. Li, Cancer-cell-biomimetic nanoparticles for targeted therapy of homotypic tumors, Adv. Mater. 28 (2016) 9581–9588, https://doi.org/10.1002/adma.201602173.

[41] A.V. Kroll, R.H. Fang, Y. Jiang, J.R. Zhou, X.L. Wei, C.L. Yu, J. Gao, B.T. Luk, D. Dehaini, W.W. Gao, L.F. Zhang, Nanoparticulate delivery of cancer cell membrane elicits multiantigenic antitumor immunity, Adv. Mater. 29 (2017), https://doi.org/10.1002/adma.201703969, 10.1002/adma.201703969.

[42] R. Roy, D. Kumar, B. Chakraborty, C. Chowdhury, P. Das, Apoptotic and autophagic effects of Sesbania grandiflora flowers in human leukemic cells, PLoS One 8 (2013), e71672, https://doi.org/10.1371/journal.pone.0071672.

[43] Y.H. Lee, F.Y. Cheng, H.W. Chiu, J.C. Tsai, C.Y. Fang, C.W. Chen, Y.J. Wang, Cytotoxicity, oxidative stress, apoptosis and the autophagic effects of silver nanoparticles in mouse embryonic fibroblasts, Biomaterials 35 (2014) 4706–4715, https://doi.org/10.1016/j.biomaterials.2014.02.021.

[44] T.J. Ji, Y. Zhao, Y.P. Ding, G.J. Nie, Using functional nanomaterials to target and regulate the tumor microenvironment: diagnostic and therapeutic applications, Adv. Mater. 25 (2013) 3508–3525, https://doi.org/10.1002/adma.201300299.

[45] X.L. Guo, N.D. Yang, W.H. Ji, H. Zhang, X. Dong, Z.Q. Zhou, L. Li, H.M. Shen, S. Q. Yao, W. Huang, Mito-Bomb: targeting mitochondria for cancer therapy, Adv. Mater. 33 (2021), e2007778, https://doi.org/10.1002/adma.202007778.

[46] H.B. Hou, X.H. Huang, G.Q. Wei, F.N. Xu, Y. Wang, S.B. Zhou, Fenton reaction-assisted photodynamic therapy for cancer with multifunctional magnetic nanoparticles, ACS Appl. Mater. Interfaces 11 (2019) 29579–29592, https://doi.org/10.1021/acsami.9b09671.

[47] N.A. Marcondes, S.R. Terra, C.S. Lasta, N.R.C. Hlavac, M.L. Dalmolin, L.A. Lacerda, G.A.M. Faulhaber, F.H.D. Gonzalez, Comparison of JC-1 and MitoTracker probes for mitochondrial viability assessment in stored canine platelet concentrates: a flow cytometry study, Cytometry 95 (2019) 214–218, https://doi.org/10.1002/cyto.a.23567.

[48] J. Doherty, E.H. Baehrecke, Life, death and autophagy, Nat. Cell Biol. 20 (2018) 1110–1117, https://doi.org/10.1038/s41556-018-0201-5.

[49] C. Münch, I. Dikic, Hitchhiking on selective autophagy, Nat. Cell Biol. 20 (2018) 122–124, https://doi.org/10.1038/s41556-018-0036-0.

[50] A.L. Anding, E.H. Baehrecke, Cleaning house: selective autophagy of organelles, Dev. Cell 41 (2017) 10–22, https://doi.org/10.1016/j.devcel.2017.02.016.

[51] Z.M. Xiao, W.B. Zuo, L.P. Chen, L. Wu, N. Liu, J.X. Liu, Q.Y. Jin, Y.L. Zhao, X. Zhu, H2O2 self-supplying and GSH-depleting nanoplatform for chemodynamic therapy synergetic photothermal/chemotherapy, ACS Appl. Mater. Interfaces 13 (2021) 43925–43936, https://doi.org/10.1021/acsami.1c10341.

[52] M.Y. Liu, D. Wang, Y.D. Luo, L.H. Hu, Y.W. Bi, J.T. Ji, H.J. Huang, G.Q. Wang, L. Zhu, J.J. Ma, E. Kim, C.K. Luo, J.L. Abbruzzese, X.K. Li, V.W. Yang, Z.S. Li, W. Q. Lu, Selective killing of cancer cells harboring mutant RAS by concomitant inhibition of NADPH oxidase and glutathione biosynthesis, Cell Death Dis. 12 (2021) 189, https://doi.org/10.1038/s41419-021-03473-6.

[53] X.W. Wang, X.Y. Wang, X.Y. Zhong, G.Q. Li, Z.J. Yang, Y.H. Gong, Z. Liu, L. Cheng, V-TiO2 nanospindles with regulating tumor microenvironment performance for enhanced sonodynamic cancer therapy, Appl. Phys. Rev. 7 (2020) 41411–41421, https://doi.org/10.1063/5.0027606.

[54] S.Y. Li, H. Cheng, B.R. Xie, W.X. Qiu, J.Y. Zeng, C.X. Li, S.S. Wan, L. Zhang, W. L. Liu, X.Z. Zhang, Cancer cell membrane camouflaged cascade bioreactor for cancer targeted starvation and photodynamic therapy, ACS Nano 11 (2017) 7006–7018, https://doi.org/10.1021/acsnano.7b02533.

[55] G.S. Song, X.C. Zheng, Y.J. Wang, X. Xia, S. Chu, J.H. Rao, A magneto-optical nanoplatform for multimodality imaging of tumors in mice, ACS Nano 13 (2019) 7750–7758, https://doi.org/10.1021/acsnano.9b01436.

[56] H.Y. Fang, M.T. Li, Q.Y. Liu, Y.K. Gai, L.J. Yuan, S. Wang, X. Zhang, M. Ye, Y. X. Zhang, M.Y. Gao, Y. Hou, X.L. Lan, Ultra-sensitive nanoprobe modified with tumor cell membrane for UCL/MRI/PET multimodality precise imaging of triple-negative breast cancer, Nano-Micro Lett. 12 (2020) 62, https://doi.org/10.1007/s40820-020-0396-4.

[57] Y.L. Lv, M. Liu, Y. Zhang, X.F. Wang, F. Zhang, F. Li, W.E. Bao, J. Wang, Y.L. Zhang, W. Wei, G.H. Ma, L.C. Zhao, Z.Y. Tian, Cancer cell membrane-biomimetic nanoprobes with two-photon excitation and near-infrared emission for intravital tumor fluorescence imaging, ACS Nano 12 (2018) 1350–1358, https://doi.org/10.1021/acsnano.7b07716.